Digest Journal of Nanomaterials and Biostructures Vol. 20, No. 4, October-December 2025, p. 1325-1344

Photoelectrothermal assisted superhydrophobic coating based on graphene/PTFE/epoxy resin

D. X. Zhang, W. Li *, A. Abbas, A. Amirfazli, Z. H. Huang
School of Materials Engineering, Jiangsu University of Technology, Changzhou 213001, China

Surface icing poses serious challenges across multiple sectors including aviation, transportation infrastructure, and building construction. While superhydrophobic coatings demonstrate ice-delaying capabilities through their water-repellent characteristics, their performance becomes limited under severe cold conditions. Similarly, electrothermal anti-icing coatings show effective ice prevention, though their application is constrained in scenarios with unreliable power supply.In this study, a photo-thermo-assisted superhydrophobic coating (SRPC) based on graphene/polytetrafluoroethylene (PTFE)/epoxy resin was developed for 7075 aluminum alloy surface. The coating was prepared by spraying method and exhibited excellent photo-thermal, electro-thermal, and anti-/de-icing properties.In terms of thermal performance, the surface temperature of the sample can reach nearly 40℃ after 8 minutes of energization, showing good thermal conversion efficiency. In terms of photothermal properties, due to the unique microstructure of the superhydrophobic coating surface and the excellent photothermal properties of graphene, the reflectivity of the samples is less than 10% and the transmittance is within 1.8%. Under 1 sun illumination, the surface heats to 88.5°C in 280 seconds and melts ice in 288 seconds. Combining 1.5 sun irradiation with 2W power reduces de-icing time to 169 seconds. These results underscore the strong potential of the fabricated coating for efficient anti-/de-icing applications in extreme environments.

(Received July 4, 2025; Accepted October 20, 2025)

Keywords: Spraying method, Optical/electrical heating, Superhydrophobic, Anti-/de-icing, Durability

1. Introduction

The severe winter conditions with snow accumulation pose significant challenges to modern industry and daily life, leading to ice formation on airplane wings, high-voltage transmission lines, and urban roads[1]. Conventional de-icing methods, including mechanical removal, chemical de-icing agents, and hot air blowing, are widely employed but suffer from inefficiency, environmental hazards, and high energy consumption. Therefore, it is essential to develop an economical, efficient, environmentally friendly, and low-energy de-icing strategy[2].

* Corresponding author: lwjslg@126.com
https://doi.org/10.15251/DJNB.2025.204.1325

Inspired by natural phenomena, scientists have developed artificial superhydrophobic coatings that, when applied to ice-prone surfaces, can prevent ice adhesion or reduce its bonding strength, facilitating easier removal[3]. However, conventional superhydrophobic coatings may lose effectiveness under extreme cold and icing conditions. To overcome this limitation, two key strategies– photothermal conversion and electrical heating–have been introduced to enhance anti-/de-icing performance[4]. Photothermal conversion materials absorb energy from sunlight or other light sources, generating localized heat through mechanisms such as plasmon resonance, electronic structure modulation, or nanomorphology design, thereby accelerating ice melting[5-8]. Alternatively, the electrical heating approach involves embedding conductive materials within the coating and generating Joule heat through voltage application, which raises the surface temperature[9]. Both methods can achieve efficient de-icing performance without compromising the integrity of the underlying substrate.

Sun et al. [10]demonstrated a rapid photothermal response, by leveraging the localized surface plasmon resonance (LSPR) effect of silver nanoparticles (AgNPs) and the intrinsic thermal vibration of carbon-based materials.They fabricated two photothermal superhydrophobic surfaces, Cu - Ag and Cu - CNT, using a simple and fast method. These surfaces-maintained droplet non-freezing in cold environments and efficiently melted ice upon illumination, even after the droplet froze without light exposure. Li et al.[11]optimized the ratio of CNTs to SiO_2 to impart optimal wettability and mechanical durability to the coating. To overcome the inherent limitations of poor wettability and mechanical durability in alloy surface coatings, a comprehensive characterization was conducted, encompassing morphological analysis, wettability assessment, mechanical robustness testing, as well as evaluations of self-cleaning capability and anti-icing performance. Yin et al.[12] incorporated Fe3O4 nanoparticles into SLIPS, combining the photothermal effect with SLIPS to delay icing and achieve photothermal de-icing, a promising active-passive combined anti-icing strategy. Antonini et al.[13]evaluated the anti-icing efficiency of superhydrophobic electrothermal metal coatings using an ice wind tunnel and found that combining superhydrophobic surfaces with electrothermal techniques can cut energy consumption for anti-icing by up to 50% [14-17]. Conventional electrothermal anti-icing and de-icing approaches are known for their high energy demands[18]. Moreover, the limited thermal conductivity and poor low-temperature tolerance of composite materials can lead to potential damage to the substrate[19-21]. Consequently, there is a pressing need to develop more energy-efficient and reliable anti-icing and de-icing strategies. This study aims to combine photothermal and electrothermal effects to enhance energy conversion efficiency. Although photothermal/electrothermal superhydrophobic coating offer significant advantages, translating them into practical applications presents several challenges. Firstly, material durability is a primary consideration for outdoor use[22-24]. Coating must withstand harsh environmental conditions, such as strong winds, acid rain, UV radiation, requiring sufficient mechanical strength and chemical stability. Secondly, energy consumption must be minimized to ensure both economic and environmental sustainability[25]. Moreover, scaling up the production of these coatings is also a key issue in industrialization, which requires the processes to be simple, cost-effective, and environmentally friendly. These challenges require urgent attention from the scientific community[26-28].

In this study, a composite coating is successfully prepared using a simple spraying technique. To evaluate the performance of this composite material, its surface wettability, conductivity, mechanical and chemical stability, as well as electrothermal and photothermal

properties are characterized and tested. The study focused on exploring the coating's anti-icing/de-icing performance in various scenarios[29].

2. Experimental

2.1. Materials

Bisphenol an epoxy resin (model: E51, epoxy equivalent: 180~200 g/mol) and curing agent (polyetheramine D230) were sourced from Zilai Adhesive factory (Shenzhen, China). N,N-dimethylformamide (DMF) was selected as the aprotic polar solvent.It was Jiangsu Lubang New Material Technology Co., Ltd. (Nanjing, China). Multilayer graphene (particle size: 7.00-10.00 μm) was purchased from Suiheng Graphene Technology (Guangzhou, China). The modifying reagent FAS-17 (perfluorodecyltriethoxysilane) was obtained from Shenlan Reagents (Quzhou, China). Polytetrafluoroethylene (PTFE) powder was purchased from Yixin Plasticization (Dongguan, Guangdong). Anhydrous ethanol (analytically pure) was obtained from Beijing Chemical Factory. All chemicals were used as received without additional purification. Deionized (DI) water was used in all experiments. All materials were used directly without further purification.

2.2. Sample preparation

Preparation of the spraying solution: firstly, the resin was dissolved using DMF as a diluent and stirred with a rod until completely dissolved. Subsequently, the curing agent, graphene powder, and modifier FAS-17 (1% by weight of the epoxy resin) were enhanced. Then the prepared mixture was magnetically stirr for 1 hour (rotation speed of 500 r / min) to obtain a graphene-epoxy resin dispersion. At the same time, polytetrafluoroethylene (PTFE) nanopowders were dispersed in anhydrous ethanol at a ratio of 1: 20 and stirred for 1 hour (600 r / min) to obtain nanoparticle dispersions. After 1 hour, the nanoparticle dispersion was added to the graphene-epoxy resin dispersion and magnetically stirred for another 1 hour (at a speed of 600 r/min). The solution was then vacuumed for 10 minutes to remove any bubbles, resulting in the final spraying solution. The weight ratio of epoxy resin/curing agent/graphene/PTFE/DMF/anhydrous ethanol was 3:1:1.5:3:9:20. By varying the mass fractions of graphene and PTFE nanoparticles, different concentrations of the spraying solution were prepared.

Preparation of the photo/electrically heated superhydrophobic coating: Initially, a layer of double-sided adhesive tape was affixed to a 7075-aluminum plate measuring 30 × 40 mm with a thickness of 1 mm. Conductive copper foil was then parallelly affixed to both sides of the aluminum plate. The double-sided adhesive tape not only fixed the copper foil to the aluminum plate surface but also acted as an insulator, isolating the coating from the aluminum substrate to protect it from damage. It also facilitated the adhesion of the subsequent spraying solution to the surface, forming a superhydrophobic coating. The aluminum plate was sprayed with different mass fractions of the spraying solution using a spray gun and then cured in an oven at 80 °C for 5 hours to prepare nano-particle photo/electrically heated superhydrophobic coatings with different mass fractions. The photo/electrically heated superhydrophobic coating prepared according to the above proportions was named SRPC. For comparison, a coating without PTFE powder was named RPC. The sample fabrication process is depicted in Figure 1.

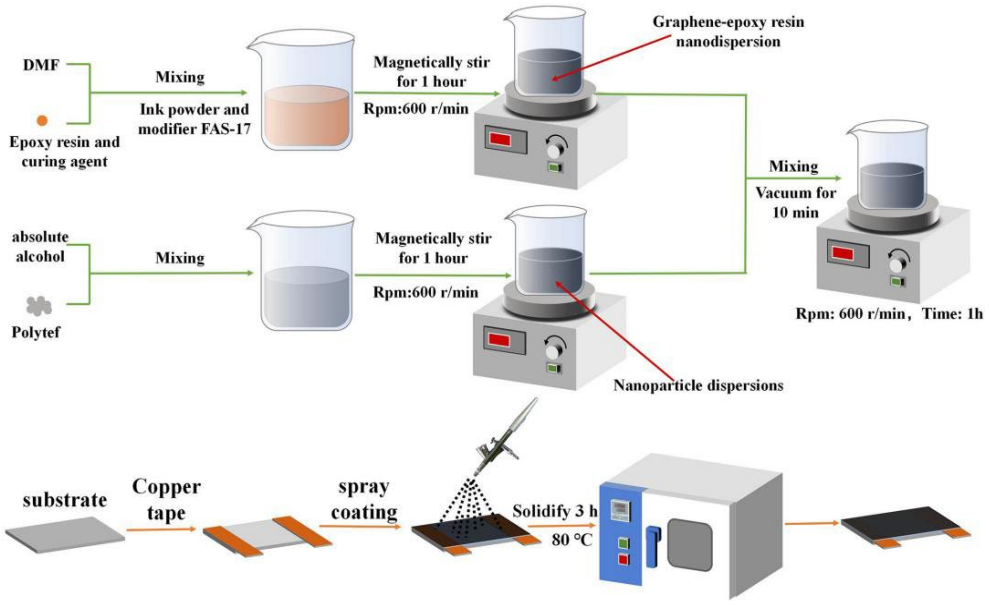

Fig. 1. Flowchart for the preparation of photo/electrically heated superhydrophobic surfaces.

2.3. Characterizations

The surface morphology of the fabricated samples was examined using field-emission scanning electron microscopy (FE-SEM; Novananosem, USA). Additionally, elemental composition was analyzed with an integrated energy-dispersive X-ray spectroscopy (EDS/EDX) system (Novananosem, USA) to provide complementary insights. Surface wettability properties were quantitatively evaluated using a contact angle goniometer (DSA 30, Krüss, Germany) under standardized measurement conditions, where 10 μL ultrapure water droplets were deployed as the probing medium for hydrophilicity assessment. The final contact angle data were obtained by averaging measurements taken at three distinct positions across three replicate samples. Sample surface temperature variations were monitored using a FLUKE P20MAX/W infrared thermal imager to evaluate photothermal conversion efficiency. A SHIMADZU UV-3900 spectrophotometer was employed to evaluate the samples' light absorption and transmission behavior. The ice formation resistance and active ice removal efficiency of the specimens were evaluated through systematic lyophilization cycles performed on a programmable freeze-drying system (Labconco FreeZone Triad, USA) under controlled temperature conditions (-50° C to 25° C) and reduced pressure (0.05 mBar) to simulate extreme icing environments and an adjustable DC regulated power supply, and a low temperature test device.

3. Results and discussion

3.1. Electrical conductivity, wettability, and compositional characterization

Composite coatings with different proportions of graphene nanopowder and PTFE pellets were prepared, and the effects of particle content on the coating's electrical conductivity and

wettability were investigated. As shown in Figure 2(a), Graphene powder to epoxy resin mass ratio increased from 0.1 to 0.6, resulted in corresponding increase in the electrical conductivity increased from 0.0015 S/m to 0.82 S/m. When the mass ratio of graphene powder to epoxy resin was 0.5, the coating had an electrical conductivity of 0.7 S/m, Select it as the best ratio for further research. Figure 2(b) illustrates the interaction between SRPC and PTFE particles at a graphene powder mass ratio of 0.5. The coating without PTFE particles, referred to as RPC, did not show superhydrophobic behavior. As the PTFE particle content increased, the coating's contact angle rose while the rolling angle decreased. When the PTFE-to-epoxy resin mass ratio reached 1, the SRPC coating exhibited a contact angle of 160.2° and a rolling angle below 5°, indicating outstanding superhydrophobicity. Additionally, with graphene and PTFE particle mass ratios of 0.5 and 1 relative to resin, respectively, the coatings demonstrated both excellent electrical conductivity and superhydrophobic performance. Based on these results, this specific mass ratio was selected for further detailed property investigations.

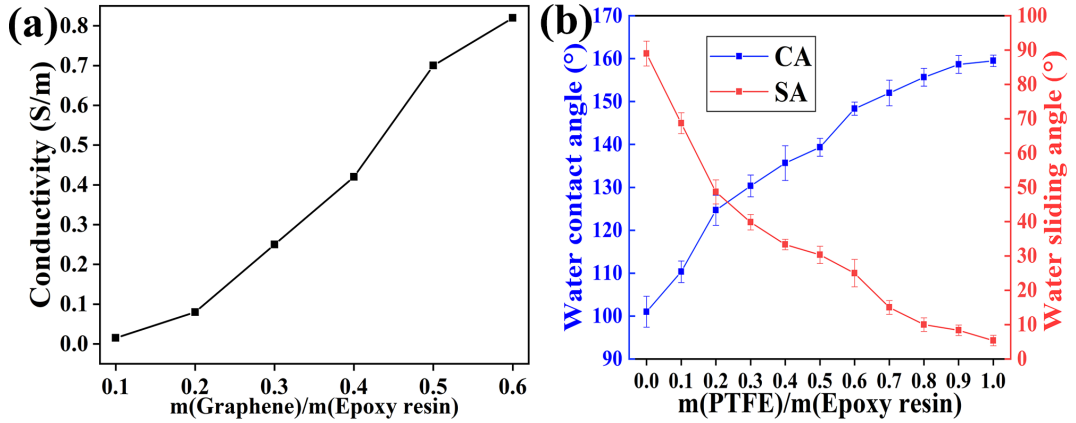

Fig. 2. (a) Curve of electrical conductivity varying with the mass ratio of graphene to epoxy resin. (b) Curve of contact angle and rolling angle varying with the mass ratio of PTFE to epoxy resin.

Figure 3 displays the FE-SEM images of RPC and SRPC at different magnifications. As seen in Figure 3(a1-a3), the surface structure of RPC is smooth, lacking sufficient nanoscale features, and has a high surface energy, resulting in a low contact angle and thus exhibiting non-hydrophobic properties. On the other hand, after the addition of PTFE to SRPC, which inherently possesses extremely low surface energy and excellent hydrophobic properties, the surface energy of the sample is significantly reduced, thereby enhancing its hydrophobic performance. As observed in Figure 3(b1-b3), the surface structure of SRPC features complex micro- or nanoscale roughness. The synergistic effect between the micro-scale roughness and PTFE's inherent low surface energy properties facilitates the formation of a surface with superhydrophobic characteristics. The hierarchical micro/nanostructure enhances air entrapment at the solid-liquid interface, creating a composite contact zone that minimizes actual liquid-solid interaction. This interfacial engineering results in contact angle elevation beyond 150°, demonstrating Cassie-Baxter-type non-wetting behavior.

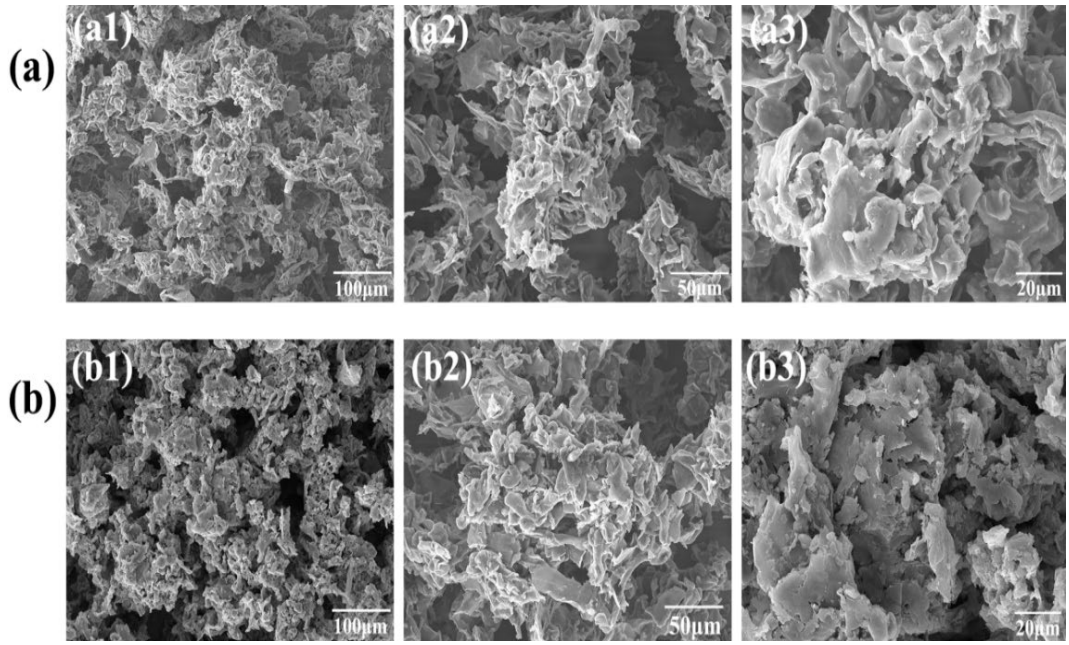

Fig. 3. Shows the Scanning Electron Microscope (SEM) screenage of RPC and SRPC specimens at different magnifications. (a) presents the surface SEM image of the RPC sample, with (a1-a3) showing images at different magnifications; (b) presents the surface SEM image of the SRPC sample, with (b1-b3) showing images at different magnifications.

EDS spectrum analysis (Figure 4) indicates that the surface of the SRPC sample primarily contains three characteristic elements: C, O, and F, with mass 60.5 wt% of the fraction, 31.3 wt%, and 6.5 wt%, respectively. Based on the composition analysis of the material system, the C and O elements mainly originate from the graphene sheets and epoxy resin matrix, while the presence of F elements is closely related to the introduction of heptadecafluoro-1,1,2,2-tetrahydrodecyl triethoxysilane (FAS-17) during the surface modification process. The element distribution maps in the energy spectrum (Figure 4a-c) clearly show the uniform distribution of each element on the material surface, with a high concentration of C element signals (60.5 wt%) confirming the dominant role of graphene in the composite coating. The results demonstrate the formation of a dense composite protective layer formed by graphene and fluorinated epoxy resin,which effectively,successfully covers the substrate surface.

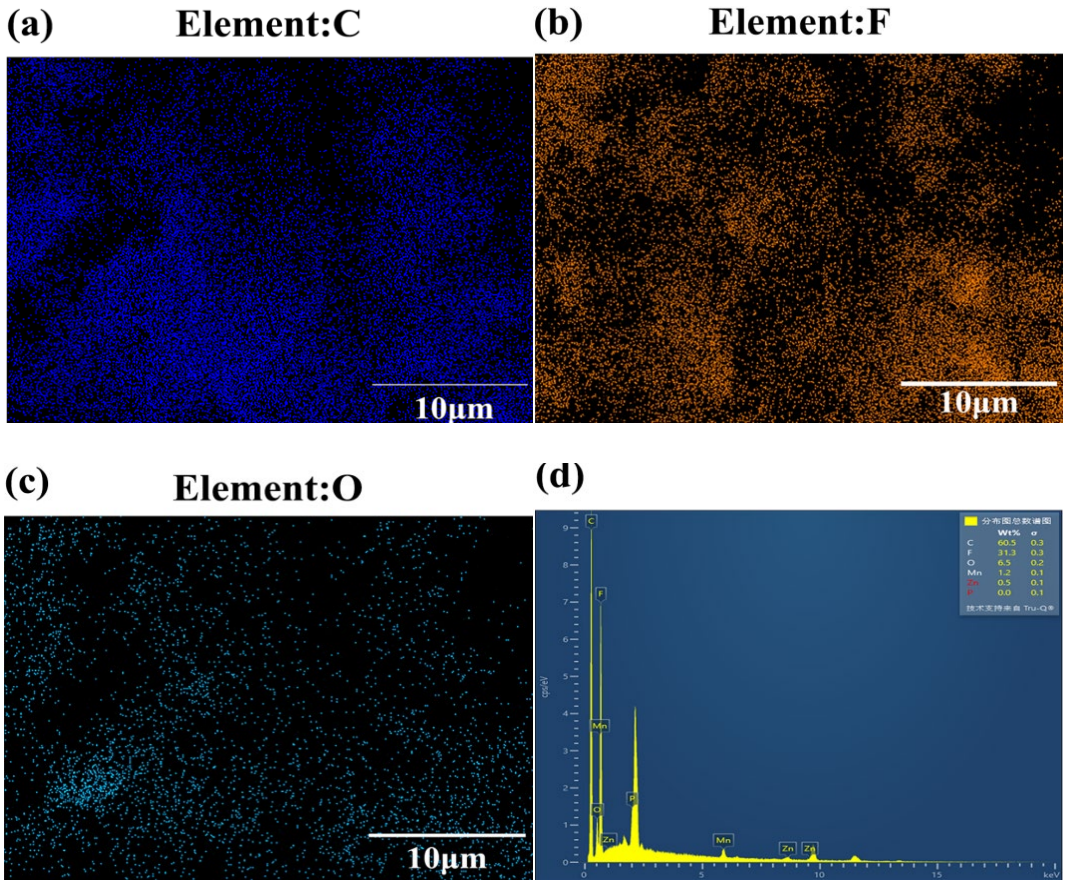

Fig. 4. shows the EDS images of SRPC. (a), (b), and (c) are the mapping images of C, F, and O elements, respectively. (d) is the overall surface spectrum.

3.2. Mechanical and chemical stability

To verify that the mechanical properties of the coating are stable, water flow and sand impact tests were conducted on the SRPC, with the test methods illustrated in Figures 5a and 5c. The SRPC was fixed on a 45° incline at a height of 10 cm, and water flowed onto the surface at a rate of 10 ml/s, and the contact angle on the SRPC surface was recorded at 5-minute intervals. Over 25 minutes of continuous water exposure, the contact angle dropped from 164.1° to 148.5°, resulting in the loss of the surface's superhydrophobic characteristics, as illustrated in Figure 5b. Similarly, for the sand impact test, the SRPC was fixed on a 45° incline, and its surface was impacted by sand particles (size of 0.5-1 mm) from a height of 20 cm. Each test used 40g of sand, and the measured sand flow rate was 10g/s. The test was conducted in cycles of 5 impacts, with a total of 5 cycles performed. After 5 cycles of sand impact, angle of contact on the SRPC surface membrane decreased from 161.5° to 149.3°, also resulting in the loss of superhydrophobicity, as shown in Figure 5d. The experimental results indicate that the SRPC exhibits good mechanical stability. This can be attributed to the fact that epoxy resin, as a binder, can effectively bond graphene and PTFE powder together to form an integrated structure, thereby enhancing the mechanical stability of the coating. It also fills the gaps between graphene and PTFE powder, reducing internal defects in the coating and further enhancing its density and hardness. Moreover,

PTFE has an extremely low friction coefficient, which endows the coating with better self-lubricating properties, reducing wear on the coating from external forces to some extent and improving its wear resistance and durability. The enhanced wear resistance of the material lays a solid foundation for its potential application in future outdoor applications.

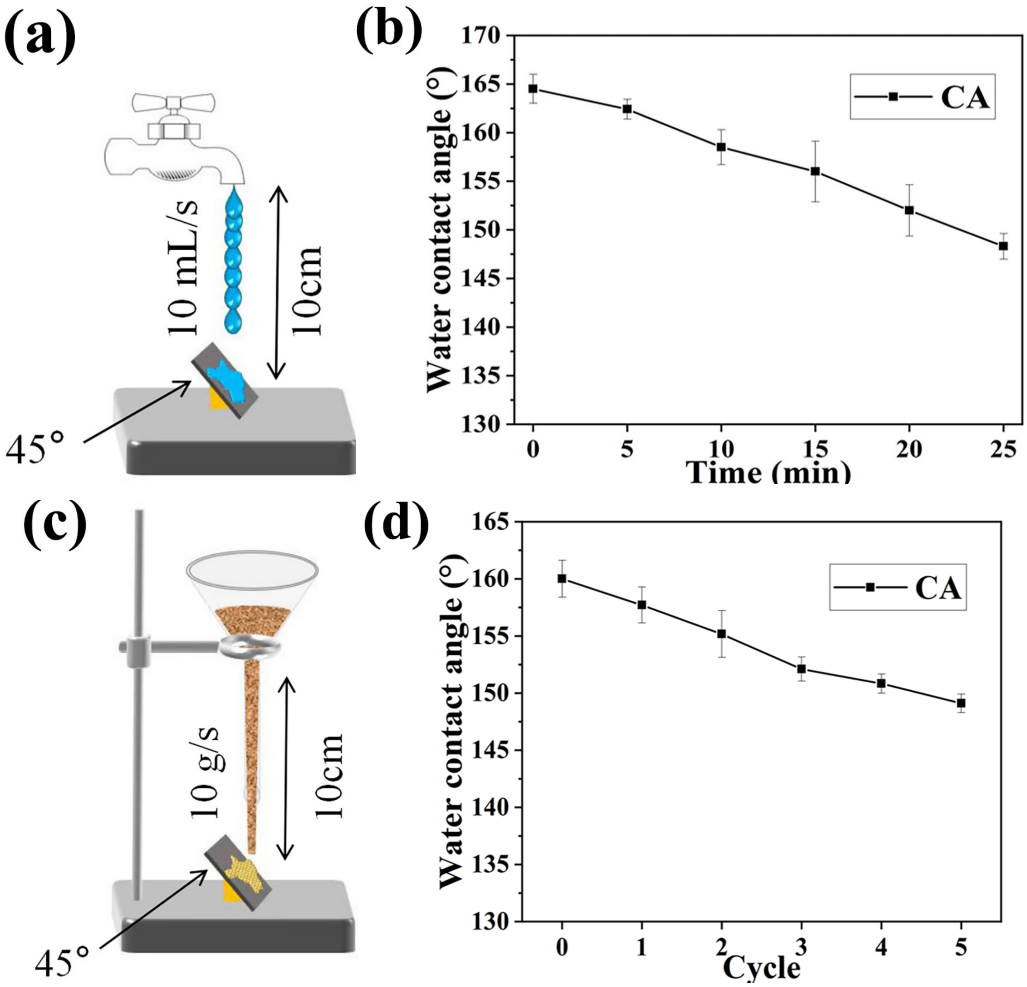

Fig. 5. (a) and (c) illustrate the schematic diagrams of water flow and sand impact on the SRPC surface. Figures 5 (b) and (d) demonstrates the images of contact angle changes on the SRPC surface.

Airborne salts and other corrosive substances may accelerate the aging and damage of coatings. To ensure long-term stable outdoor use of the coating, the acid-base resistance of the SRPC coating was tested. The samples were immersed in HCl (p H = 3) and NaOH (p H = 13) solutions, the number of contact angles of the SRPC was measured every two hours. The results are shown in Figures 6(a) and 6(b). After 12 hours in the HCl solution, the contact angle of the sample degrees from 162.2° to 151.3°. In the NaOH solution, water contact angle of the sample reduced from 161.5° to 154.1°. Whether immersed in the HCl solution with pH 3 or the NaOH solution with a pH of 13, the contact angle only decreased slightly after 12 hours, and the superhydrophobicity of the coating was not lost. On one hand, due to the special microstructure of the superhydrophobic coating, which forms an air cushion that prevents water from staying on the

coating's surface, thereby avoiding direct contact between water and the coating's interior. This design not only enhances the coating's hydrophobicity but also strengthens its resistance to acidic and alkaline solutions. On the other hand, the incorporation of graphene and PTFE further enhances the coating's acid and alkali resistance, enabling it to exhibit good stability when exposed to acidic and alkaline solutions.

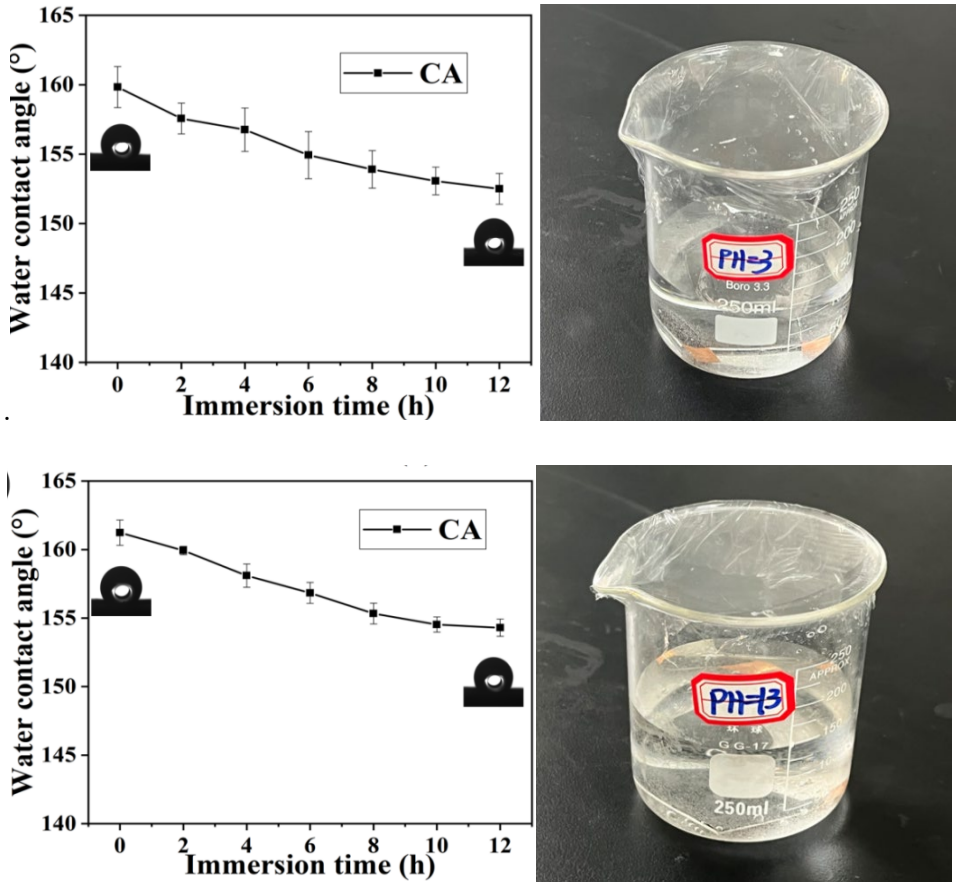

Fig. 6. (a) Shows the image and experimental diagram of the contact angle change over time for SRPC immersed in HCl solution. (b) shows the image and experimental diagram of the contact angle change over time for SRPC immersed in NaOH solution.

To study the effect of UV radiation on the surface of SRPC coating, place the SRPC in an accelerated UV aging chamber for 10 days of UV exposure. The contact angle of the samples was measured every two days, with the results presented in Figure 7. As shown in the figure 7, the contact angle of the SRPC remain in relatively Stabilized at about 160° throughout the 10-day exposure period. This stability is primarily attributed to graphene's unique two-dimensional structure and electronic properties, which absorb and scatter a significant amount of light, reducing the damage caused by UV light to the coating. Additionally, PTFE powder possesses good UV resistance, contributing to the maintenance of the coating's performance.

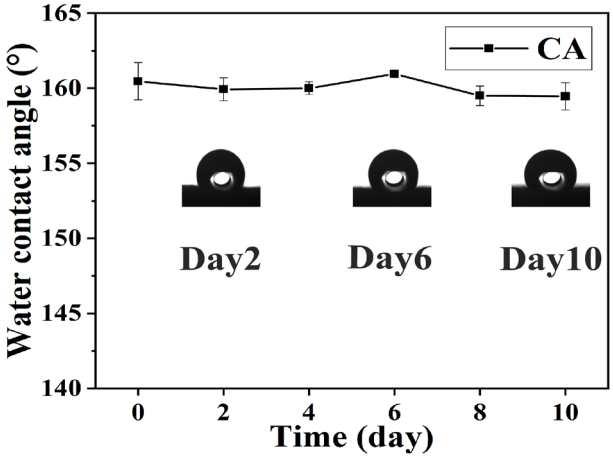

Fig. 7. Image showing the alteration in contact angle of the SRPC surface over time during the UV aging test.

3.3. Electrothermal properties of RPC and SRPC coatings

To test the electrothermal properties of the prepared samples, both RPC and SRPC were connected to a constant voltage source of 10V, and the surface temperature of the two coatings was recorded every minute for a total of 6 minutes. The results are shown in Figure 8(a). As can be seen from the figure, after 6 minutes of continuous heating, both RPC and SRPC reached a steady-state temperature. The steady-state temperature of RPC was around 72℃, while the steady-state temperature of SRPC, which included polytetrafluoroethylene (PTFE), decreased to around 40℃[30]. This effect is attributed to the rise in electrical resistance of the coating following the incorporation of PTFE, as described by Joule's Law:

$$Q = (U^2/R)t \tag{1}$$

(Q represents the heat generated by the coating, V is the externally applied voltage, R is the resistance value of EH coating, and it is the time of electrification.) According to Joule's Law, When the voltage applied and electrification time are the same, the smaller the resistance of the coating, the more heat is generated. And the more heat generated in the same amount of time, the faster the heating rate. In the first 5 minutes, the temperature rise rate of RPC was always higher than that of SRPC. When the electrification time reached 5 minutes, the heating rate of both RPC and SRPC significantly slowed down and eventually approached zero. At the same time, the surface temperature of the coatings also stabilized at a state close to the steady-state temperature, as shown in Figure 8(b).

Furthermore, an infrared thermal imager was employed to measure and observe the temperature of the SRPC during both the initial stage of heating and once it reached the steady-state temperature, with the results presented in Figure 8(c). As presented the figure, the temperature distribution of the SRPC was very uniform both at the initial stage of heating and when it reached the steady-state temperature. This uniform temperature distribution can be credited to the exceptional electrical and thermal conductivity of graphene, along with the use of a spray coating method that ensures a more uniform distribution of the coating.

Lastly, the electrical heating stability performance of the SRPC was tested. The SRPC was connected to a constant voltage source of 15V to heat its surface to the steady-state temperature, and then the power was turned off to allow it to cool down to ambient temperature (28℃). The temperature of the SRPC surface was recorded every 60 seconds for 5 cycles of heating-cooling. The test results are shown in Figure 8(d). As you can see from the diagram, the temperature change curves for the 5 heating-cooling cycles were almost identical, indicating that the electrical heating behavior is stable and repeatable.

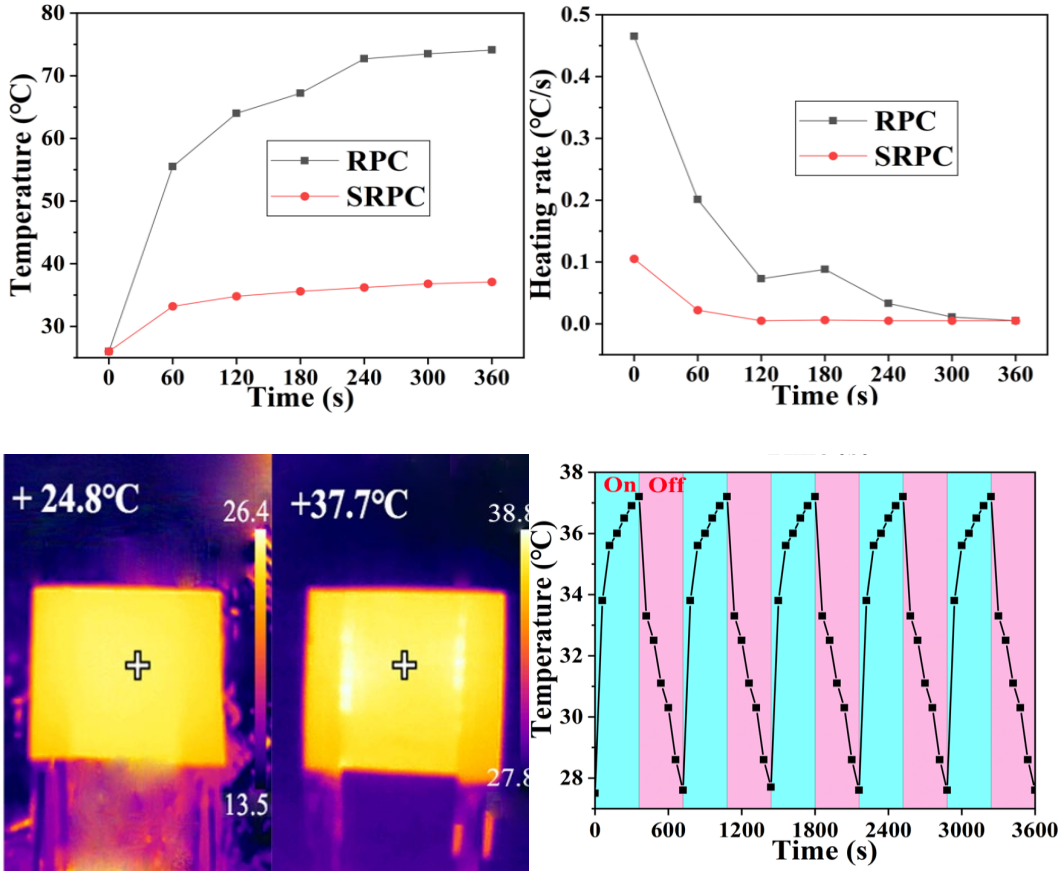

Fig. 8. (a)Heating curves of RPC and SRPC. (b) Heating rate curves of RPC and SRPC. (c) Thermal infrared images of SRPC. (d) Temperature changes of SRPC during heating-cooling cycles.

3.4. Photothermal performance of RPC and SRPC coatings

The coatings prepared in this work not only exhibit electrothermal conversion performance but also possess photothermal conversion capability. The reflectance and transmittance spectra of the RPC and SRPC coatings were analyzed using a UV-VIS-NIR spectrophotometer. Figures 9(a) and 9(b) display the spectral data for both coatings across the 200–2500 nm wavelength range. As illustrated in the reflectance spectrum in Figure 9(a), when the two coatings are exposed to light of the same wavelength, the reflectance of SRPC is lower than that of RPC. In the UV-visible light range, the reflectance of both coatings drops rapidly, with the reflectance of RPC decreasing from 18.5% to 10.9%, and that of SRPC decreasing even more

significantly from 14.6% to 9.2%. In the near-infrared range, the average reflectance of SRPC is within 10%. The transmittance spectrum in Figure (b) shows that the transmittance of both RPC and SRPC coatings is less than 2%. The low reflectance and transmittance ensure high light absorption on the sample surface.

To further verify the efficiency of the coatings in converting solar energy into thermal energy, the RPC and SRPC samples were placed under 1 sun illumination intensity (1000 W/m²) at room temperature (28°C) for 5 minutes, and temperature readings from the sample surfaces were taken at 30-second intervals. The corresponding data is shown in Figure 9(c), which clearly demonstrates that the surface temperature of both samples continued to rise steadily under the illumination. In the first three minutes, the surface temperature of RPC was slightly higher than that of SRPC. After three minutes of illumination, the temperatures of the two were very close, and neither had reached a steady-state temperature after 5 minutes, indicating that there was still room for temperature increase. However, since the actual solar illumination intensity is not constant, the heating performance of the SRPC coating was studied under three different illumination intensities. SRPC was exposed to 0.5 sunlight, 1 sunlight and 1.5 sunlight, and its surface temperature was measured and recorded within 5 minutes. The results are shown in Figure 9(d). It can be seen that the surface temperature of the sample increases as the light intensity increases. Even at the low illumination intensity of 0.5 sun, the surface temperature of SRPC rise to 68.3°C after 5 minutes, with room for further increase. At 1.5 sun illumination intensity, the temperature of SRPC reached 110.5°C. The results indicate that SRPC exhibits excellent photothermal conversion performance under different illumination intensities.

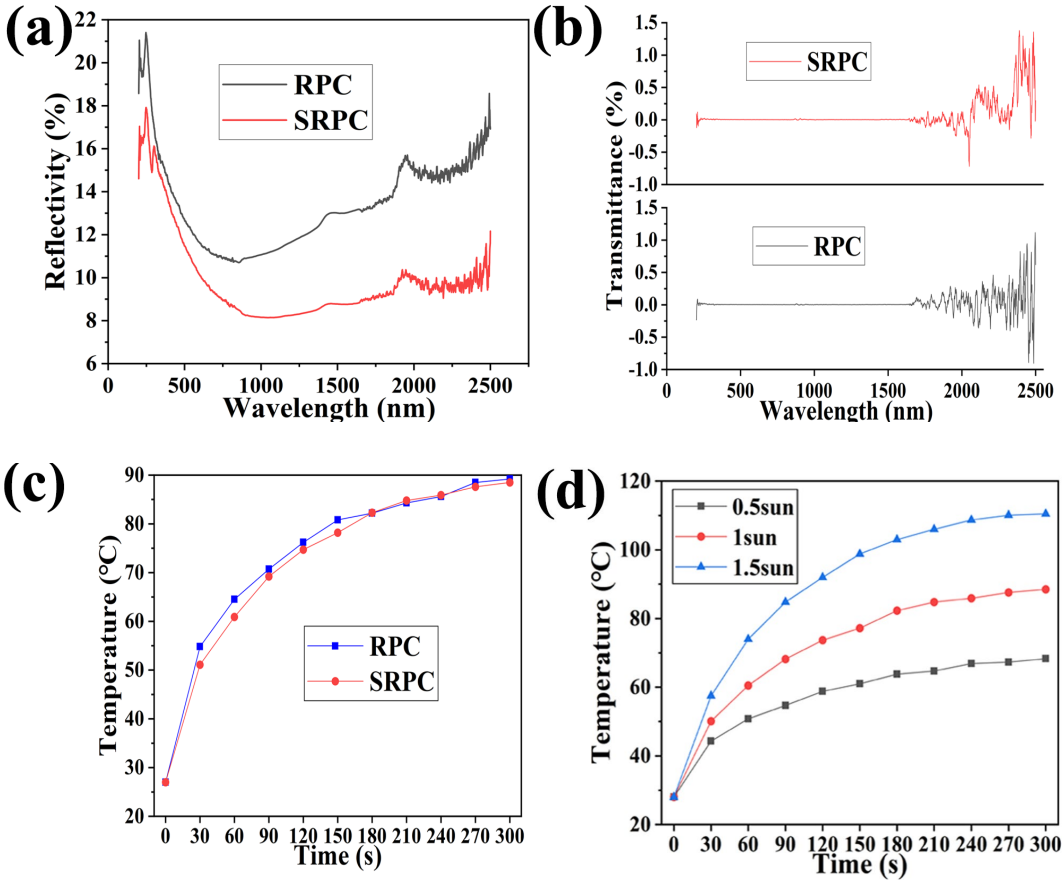

Fig. 9. (a) Reflectance spectra of RPC and SRPC. (b) Transmittance spectra of RPC and SRPC. (c) Surface temperature variation curves of RPC and SRPC over time under 1 sun illumination intensity. (d) Surface temperature variation curves of SRPC over time under different illumination intensities.

As can be seen from the thermal infrared images in Figure 10(a), the SRPC superhydrophobic coating exhibits a very uniform temperature distribution, both at the initial heating temperature of 43.3°C and at the temperature of +89.3°C after 5 minutes of heating. This uniform temperature distribution can be credited to the excellent thermal conductivity of graphene and the uniform distribution of the coating. Additionally, the photothermal stability of SRPC was tested by exposing it to 1 sun illumination intensity to heat it up, and then turning off the light source to allow it to cool down to room temperature. This process was repeated for 5 cycles of illumination-cooling, with ten data points recorded for each cycle of heating and cooling. After the surface temperature of SRPC cooled down to room temperature, the next cycle began. The test results of the samples are shown in Figure 10(b). The temperature profiles across the five heating–cooling cycles show minimal variation, indicating that SRPC has stable photothermal conversion performance.

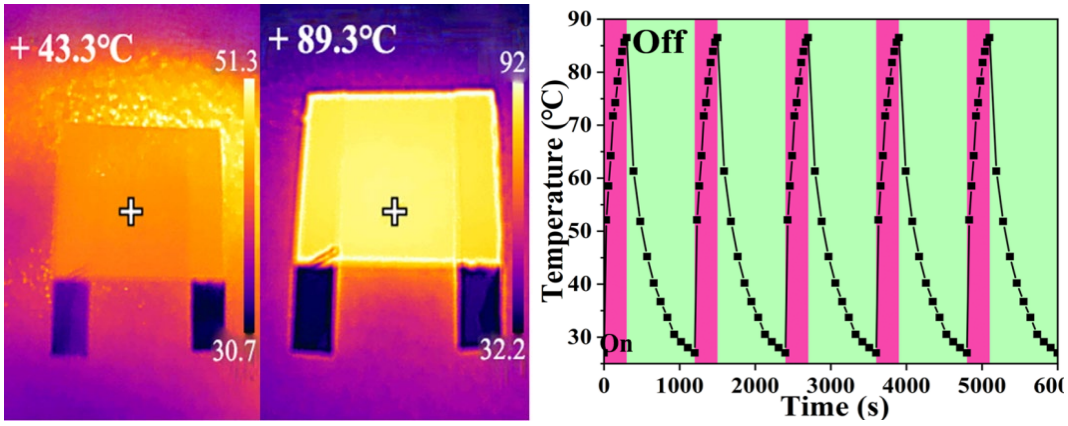

(a) *(b)*

Fig. 10. (a) Thermal infrared image of SRPC. (b) Temperature variation of the SRPC during repeated illumination and cooling cycles.

3.5. Ice-preventing performance of SRPC

The process of water freezing is generally considered to be divided into two parts: nucleation and growth. In a supercooled state, water molecules occasionally form transient, ordered ice-like structures due to random thermal motion, which are known as ice nuclei. The formation of ice nuclei is a random event, and they are usually very small and unstable. When the size of an ice nucleus grows to a certain extent, it reaches the so-called "critical ice nucleus" state. Once a critical ice nucleus is formed, other water molecules rapidly gather around it to form larger ice crystals. This phase represents the growth of ice crystals and is considered the most significant stage of the overall freezing process[31-32]. Initiating nucleation necessitates surpassing the Gibbs free energy barrier, which can be quantitatively described as follows:

$$\Delta G_C = \Delta G^* f(m, x) \tag{2}$$

$$\Delta G^* = \frac{16\pi\gamma^3}{3(\Delta G)^2} \tag{3}$$

In the equation, represents the Gibbs free energy barrier for heterogeneous nucleation, represents the Gibbs free energy barrier for homogeneous nucleation, is a geometric parameter influenced by surface wettability and morphology, and is the interfacial tension between ice and water. The reason why superhydrophobic surfaces can increase the barrier for ice crystal nucleation and prolong the nucleation time is that they alter the surface wettability and morphology. To investigate the ice-delaying performance of the materials, smooth aluminum plates, RPC, and The SRPC was placed in a cooler at -30℃, and a drop of 10 μL deionized water is added to the surface. The timing started when the temperature in the cooler dropped to 0℃, and the droplet freezing behavior on the sample surfaces was monitored as they cooled from room temperature to -30℃, as shown in Figure 11.

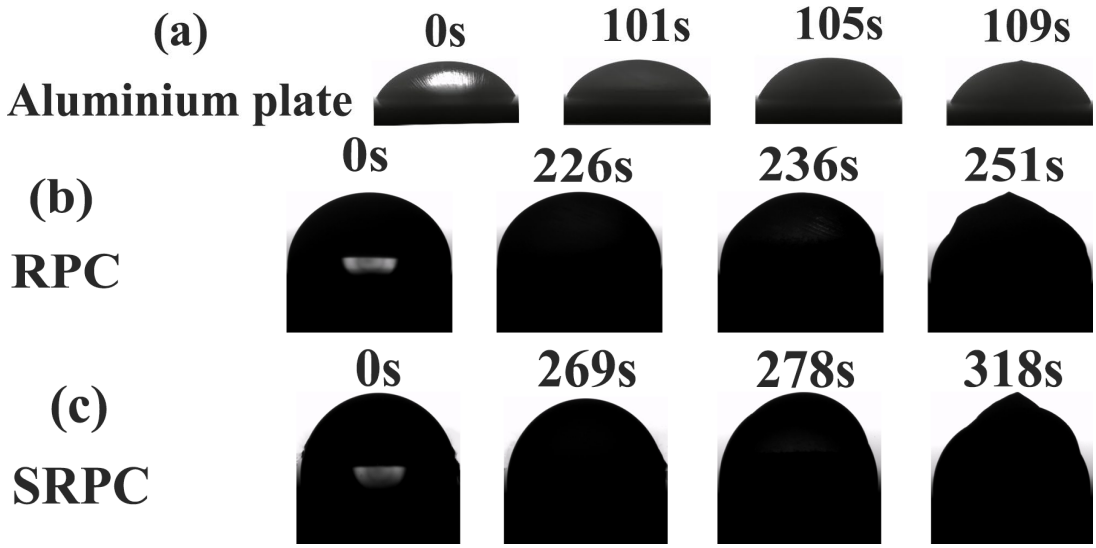

Fig. 11. (a) shows the ice formation process of a droplet on the surface of an aluminum plate, (b) shows the process by which a droplet freezes on the RPC surface, and (c) shows the ice formation process of a droplet on the surface of SRPC.

From Figure (a), it can be seen that the droplet on the smooth aluminum plate changed from a transparent water droplet to an opaque state in just 109 seconds. After another 8 seconds, the droplet completely froze, eventually forming miniature forest-like ice crystals on the surface. In contrast, by comparing Figures (b) and (c), it can be seen that the freezing time of the droplets was delayed on the surfaces with coatings, especially on the SRPC surface, where the freezing time was delayed by nearly three times. This can be attributed to two factors. On one hand, the coatings reduce the surface wettability, dramatically increase hydrophobicity, and the hydrophobic surface minimizes the solid–liquid interface, thereby slowing down heat transfer process and thus postponing the droplet's supercooling and freezing time. On the other hand, when droplets impact the multi-level micro-nano superhydrophobic surface, the air trapped by the surface structure acts as a thermal insulation, increasing the thermal resistance of liquid-solid heat transfer and thereby delaying the freezing time.

To investigate the function of light on the ice retarding effect on the surface of SRPC, SRPC was placed at -30° C and a volume of 30 μL deionized water was applied to the surface. Light of different intensities was directed onto the SRPC, and the images and times of droplet freezing were observed and recorded. The results are shown in Figure 12.

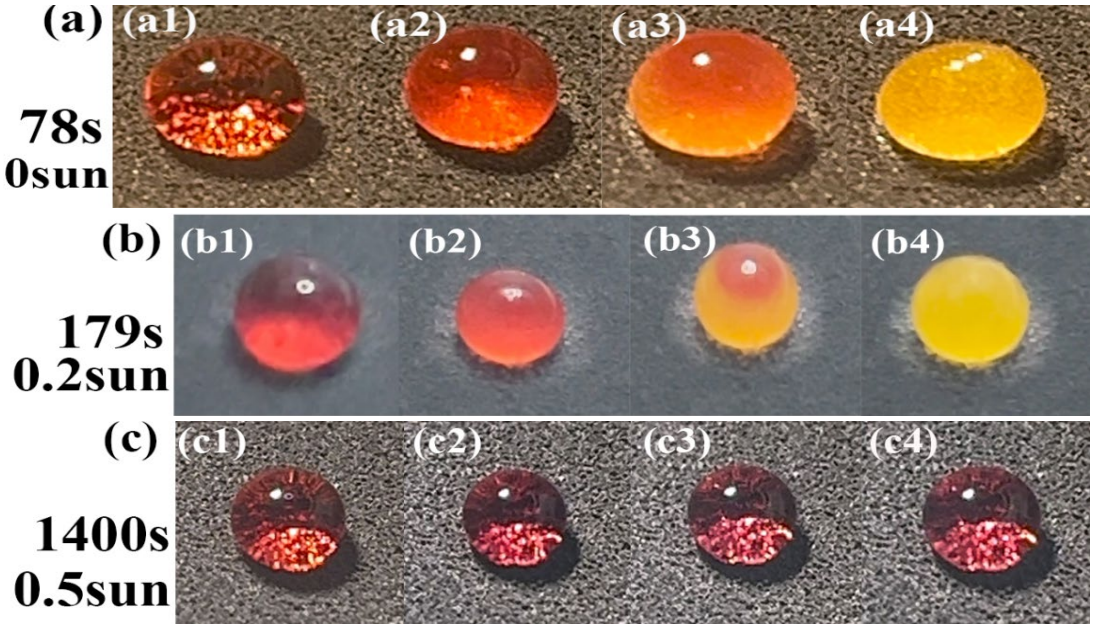

Fig. 12. Records droplet freezing on SRPC surfaces across light intensities, showing ice formation stages under varied illumination, to facilitate observation of the freezing process, phenol red was used to stain the droplets. (a) Under dark conditions, the ice nucleation and growth dynamics of water droplets on the superhydrophobic (SRPC) surface were systematically investigated. Figure panels (a1-a4) sequentially depict the transitional freezing stages of droplets at specific time intervals during illumination exposure. (b) Under 0.2 sun irradiance conditions, the crystallization dynamics of water droplets on the superhydrophobic (SRPC) surface were experimentally characterized. Image series (b1-b4) chronologically document the progressive solidification phases of droplets at defined illumination time intervals, revealing distinct ice nucleation and growth patterns under low-intensity light exposure. (c) Ice formation droplets on the SRPC under 0.5 sun light intensity, with (c1-c4) showing the freezing states of droplets on the SRPC surface at different illumination times.

As can be seen from Figure 12, in the dark, the droplet on the SRPC surface completely froze in just 78 seconds. However, under 0.2 solar light irradiation, the time for the droplet to completely freeze was extended to 179 seconds, which is nearly double the time compared to the dark environment. When the light intensity was increased to 0.5 sun, the droplet did not show any tendency to freeze even after 1400 seconds, and the droplet remained transparent.

Similarly, to investigate the effect of output power on the ice-delaying effect of the SRPC surface, different output powers were applied to the SRPC, and the images and times of droplet freezing were observed and recorded. As illustrated in Figure 13, the application of 0.5 W

extended the freezing time from 78 seconds to 85 seconds, indicating a minor delay of 7 seconds. However, when the output power was increased to 2W, the droplet did not completely freeze even after 1200s, and it remained transparent. The experimental results show that applying a certain amount of light and electrical energy to SRPC can delay the freezing time, and as the light intensity and electrical power increase, the freezing time continues to extend until there is no freezing at all.

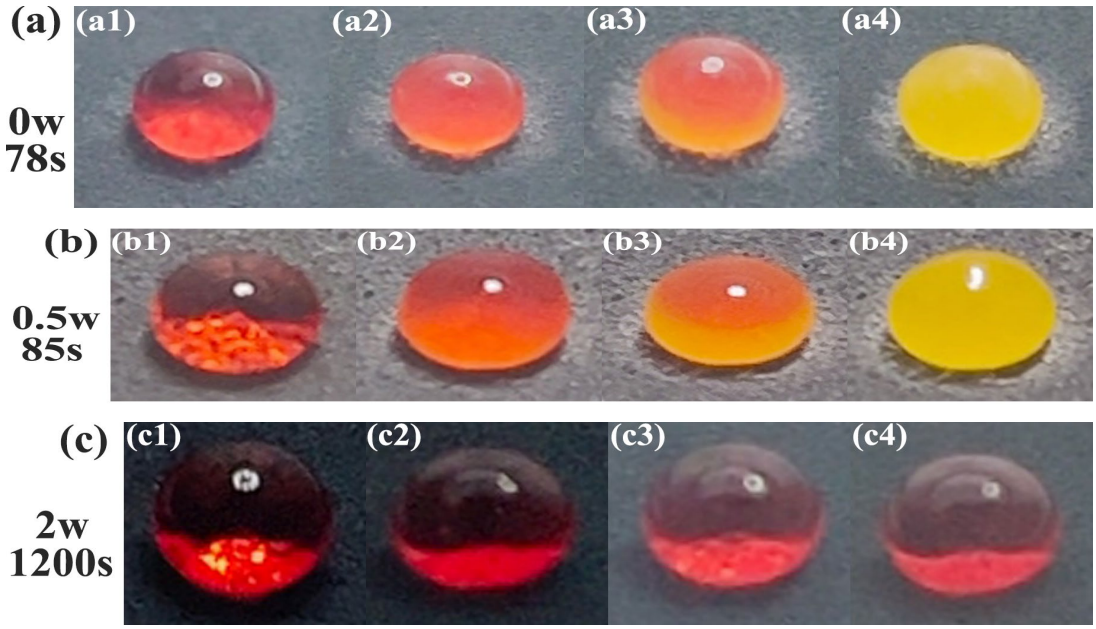

Fig. 13. Droplets on SRPC surfaces were monitored during freezing under controlled power outputs, with phenol red dye added to track crystallization stages visually. (a) The droplet's freezing behavior on the SRPC surface under zero output power conditions, (a1 ~ a4) represent the freezing state of droplets on the SRPC surface for different energization times ; (b) When the output power is 0.5 W, Ice formation process of droplets on the SRPC surface, (b1-b4) Indicates the state of a droplet at different energization times;(c) The process of droplet icing on the SRPC surface when the output power is 2W, with (c1-c4) showing the freezing states of droplets on the SRPC surface at different electrification times.

3.6. De-icing performance of SRPC

To further investigate the active de-icing of the coating surface after ice formation, a series of experiments were designed in this study, including photothermal de-icing, Joule heating de-icing, and combined photothermal and Joule heating de-icing tests. These experiments aimed to evaluate and optimize the de-icing performance of the coating under the influence of solar energy and electrical energy. To ensure consistency in experimental data, 2 mL of water was used in each round of experiments to cool and form an ice layer on the coating surface. Subsequently, the SRPC sample with the ice layer was placed in a frozen environment maintained at -30°C and allowed to reach a stable temperature. Then, different intensities of light were applied to the SRPC surface and the melting process of the ice was monitored. The time required for complete ice ablation was recorded, and the test results are shown in Figure 14.

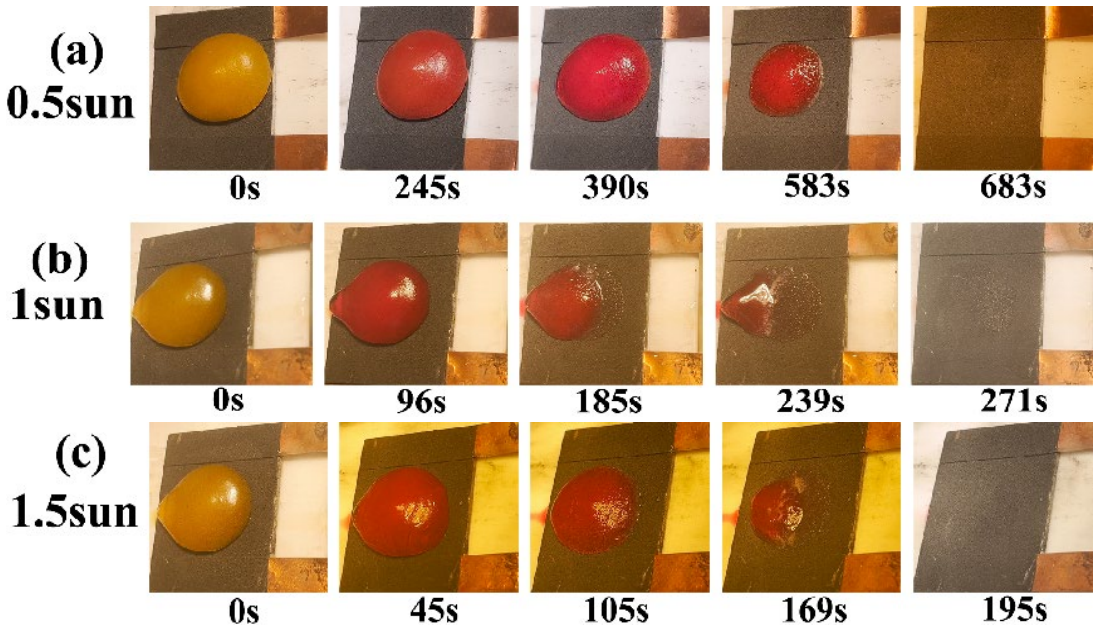

Fig. 14. The melting behavior of ice layers on SRPC surfaces under varying light intensities is demonstrated. (a), (b), and (c) represent light intensities of 0.5 sun, 1 sun, and 1.5 sun, respectively.

As seen in Figure 14, the time required for complete ice melting decreases with increasing light intensity. When exposed to light at 0.5 sun intensity, it takes 683 seconds for the ice on the SRPC surface to melt entirely. As the light intensity increases to 1 sun and 1.5 suns, reduction of the time for complete melting of the ice sheet to 271 seconds and 195 seconds, respectively. During the ice melting process, the ice was observed to begin melting from the bottom, where it was in contact with the coating, and then spread outwards. This phenomenon indicates that the SRPC surface retains strong photothermal characteristics, despite being covered by a substantial ice layer.

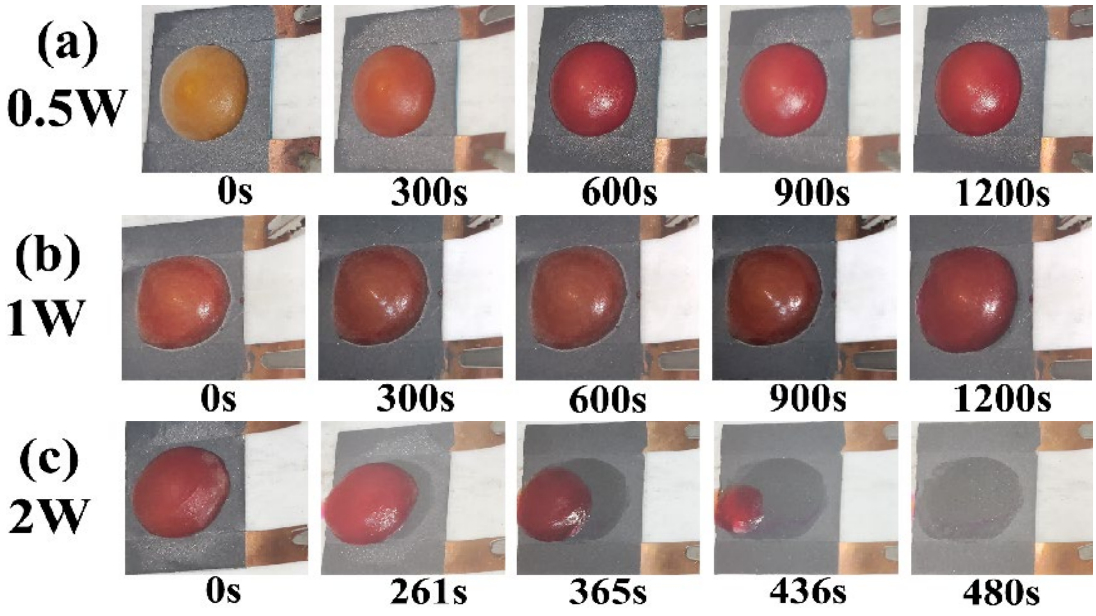

Fig. 15. Shows the ice melting process on the SRPC surface under different output powers. (a), (b), and (c) represent output powers of 0.5W, 1W, and 2W, respectively.

Replacing solar energy with electrical energy,De-icing Effectiveness of SRPC surface was further investigated under the same conditions with different output powers. The results are shown in Figure 15.

According to the figure 15, at an output power of 0.5W, the ice layer does not melt even after 1200s, but only changes from an opaque state to a transparent state at the bottom. When the output power is increased to 1W, there is still no significant melting of the ice layer after 1200s. However, when the output power is further increased to 2W, the ice layer starts to melt with water droplets appearing after 261s, and completely melts after 480s. Compared to an output power of 0.5W, the entire melting period of the ice layer is shortened by nearly 2.8 times. These results indicate that the effect of electrical de-icing is not significant at lower output powers. As the output power increases, the time for ice layer to melt on the SRPC surface shortens, and a small increase in output power can significantly enhance the de-icing phenomenon.

At the end of the experiment, to test the de-icing outcome of the combination of light energy and electrical energy, a 1.5 sun light intensity and an output power of 2W were simultaneously applied to the SRPC, and the melting progression of the ice layer was observed. The results are shown in Figure 16.

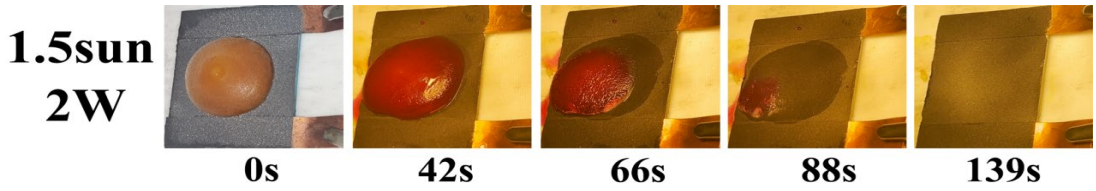

Fig. 16. The melting behavior of the ice on the SRPC surface under combined 1.5-sun light intensity and 2W output power is investigated.

Just 42 seconds after the start, significant melting was observed ice sheet bottom, with droplets forming at the top. After 88 seconds, more than half of the ice layer had melted, and by 139 seconds, the ice layer had completely melted. The experimental results indicate that compared to using light energy or electrical energy alone for de-icing, the combined use of light energy and electrical energy can further shorten the time needed for the ice layer to melt on the SRPC surface.

4. Conclusions

In this study, an innovative spraying approach has been successfully developed to prepare graphene/PTFE/epoxy resin photoelectric and auxiliary heating superhydrophobic surfaces with different proportions. The incorporation of graphene endows the material with electrical conductivity, and under an applied constant voltage of 10V, the surface temperature of the material reaches nearly 40°C after 6 minutes of electrification. The special microstructure of the superhydrophobic coating surface, coupled with the excellent photothermal properties of graphene, results in a reflectivity of less than 10% and a transmittance of less than 2% for the material. Under 1 sun illumination intensity, the surface temperature of the material rises to 88.5°C within 300

seconds. The special structure of the material surface and its optical/electrothermal properties significantly enhance its anti-icing and de-icing performance. In a low-temperature environment of -30°C, the material delays the onset of icing for up to 318 seconds, which is nearly three times longer than that of a smooth aluminum plate. De-icing test results indicate that under 1 sun illumination intensity, the surface temperature of the material rapidly increases, leading to a notable improvement in de-icing efficiency (271 seconds). When the output power is 2W, the ice layer on the material surface melts and completely disappears within just 480 seconds. Under the combined effect of 1.5 sun illumination intensity and 2W output power for de-icing, the de-icing time is further reduced to 139 seconds. Moreover, this material exhibits outstanding mechanical strength and exceptional chemical stability. coupled with remarkable UV degradation resistance, ensuring reliable performance in extended outdoor applications. These superior properties position it as an ideal candidate for deployment in high-voltage power transmission systems, wind turbine components, and similar demanding engineering applications.

Acknowledgements

The work was supported by the National Natural Science Foundation of China (52073127).

References

[1] N. Karim, M. Zhang, S. Afroj, V. Koncherry, P. Potluri, K. S. Novoselov, RSC Advances, 8 (2018) 16815; https://doi.org/10.1039/C8RA02567C

[2] L. Vertuccio, F. De Santis, R. Pantani, K. Lafdi, L. Guadagno, Composites Part B, 162 (2019) 600; https://doi.org/10.1016/j.compositesb.2019.01.045

[3] J. Fan, Z. Long, J. Wu, P. Gao, Y. Wu, P. Si, D. Zhang, Journal of Coatings Technology and Research, 20 (2023) 1557; https://doi.org/10.1007/s11998-023-00762-x

[4] B. Wu, X. Cui, H. Jiang, N. Wu, C. Peng, Z. Hu, X. Liang, Y. Yan, J. Huang, D. Li, Journal of Colloid and Interface Science, 590 (2021) 301; https://doi.org/10.1016/j.jcis.2021.01.054

[5] B. Zhang, Y. Ying, Y. Zhu, Y. Jiang, Y. Zhang, Y. Qiu, Carbon, 174 (2021) 10; https://doi.org/10.1016/j.carbon.2020.12.009

[6] Y. Qi, Z. Yang, W. Huang, J. Zhang, Applied Surface Science, 538 (2021) 148131; https://doi.org/10.1016/j.apsusc.2020.148131

[7] C. Wu, H. Geng, S. Tan, J. Lv, H. Wang, Z. He, J. Wang, Materials Horizons, 7 (2020) 2097; https://doi.org/10.1039/D0MH00636J

[8] J. Huang, S. Lu, Y. Hu, L. Liu, H. You, Coatings, 14 (2024) 758; https://doi.org/10.3390/coatings14060758

[9] P. Irajizad, A. Al-Bayati, B. Eslami, T. Shafquat, M. Nazari, P. Jafari, V. Kashyap, A. Masoudi, D. Araya, H. Ghasemi, Materials Horizons, 6 (2019) 758; https://doi.org/10.1039/C8MH01291A

[10] W. Sun, Y. T. Wei, Y. H. Feng, F. Q. Chu, et al.,Energy 286,(2024) 129656; https://doi.org/10.1016/j.energy.2023.129656

[11] Li. G, Han. Q, Yang. K, et al, Chemical Engineering Journal, 502 (2024) 157980; https://doi.org/10.1016/j.cej.2024.157980

[12] Yin. X, Zhang. Y, Wang. D, et al., Advanced Functional Materials, 25 (2015) 4237-4245; https://doi.org/10.1002/adfm.201501101

[13] Antonini C, Innocenti M, Horn T, et al., Cold Regions Science and Technology, 67 (2011) 58-67; https://doi.org/10.1016/j.coldregions.2011.02.006

[14] G. Y. Bae, J. Jang, Y. G. Jeong, W. S. Lyoo, B. G. Min, J. Colloid Interface Sci., 344 (2010) 584-587; https://doi.org/10.1016/j.jcis.2010.01.024

[15] D. Xia, L. M. Johnson, G. P. Lopez, Adv. Mater., 24 (2012) 1287-1302; https://doi.org/10.1002/adma.201104618

[16] Momen G, Jafari R, Farzaneh M. Applied Surface Science, 349(2015) 211-218; https://doi.org/10.1016/j.apsusc.2015.04.180

[17] Y. Liu, R. Xu, N. Luo, Y. Liu, Y. Wu, B. Yu, S. Liu, F. Zhou, Advanced Materials Technologies, 6 (2021) 2100371; https://doi.org/10.1002/admt.202100371

[18] L. Zhou, Y. Tan, J. Wang, et al.,Nature Photonics, 10 (2016)393-398; https://doi.org/10.1038/nphoton.2016.75

[19] S. Jiang, S. Gao, Y. Liu, et al., International Journal of Applied Ceramic Technology, 17 (2019) 130-137; https://doi.org/10.1111/ijac.13240

[20] Z. Xie, H. Wang, M. Li, et al.,Chemical Engineering Journal, 435 (2022).

[21] Q. Li, Z. Guo,et al., Journal of Materials Chemistry A, 6 (2018)13549-13581; https://doi.org/10.1039/C8TA03259A

[22] G. Jiang, L. Chen, S. Zhang, et al, ACS Applied Materials & Interfaces, 10 (2018) 36505-36511; https://doi.org/10.1021/acsami.8b11201

[23] H. Wu, X. Zhang, Z. Ma, et al., Advanced Science, 7 (2020) 1903208; https://doi.org/10.1002/advs.202003370

[24] G. Barati Darband, M. Aliofkhazraei, S. Khorsand, et al., Arabian Journal of Chemistry, 13 (2020) 1763-1802; https://doi.org/10.1016/j.arabjc.2018.01.013

[25] L. Ma, J. Wang, F. Zhao, et al,Composites Science and Technology, 181 (2019) 107696; https://doi.org/10.1016/j.compscitech.2019.107696

[26] S. Hao, Y. Zhan, W. Li, et al, Advanced Engineering Materials, 26 (2024) 2301948; https://doi.org/10.1002/adem.202301948

[27] M. J. Nine, T. T. Tung, F. Alotaibi, et al, ACS Applied Materials & Interfaces, 9 (2017) 8393-8402; https://doi.org/10.1021/acsami.6b16444

[28] X. Ni, Y. Gao, X. Zhang, et al, Chemical Engineering Journal, 406 (2021) 126725; https://doi.org/10.1016/j.cej.2020.126725

[29] D. Wang, L. Xu, L. Zhang, et al, Chemical Engineering Journal, 420 (2021) 127679; https://doi.org/10.1016/j.cej.2020.127679

[30] D. Zhang, Q. Xia, H. Lai, et al, Science China Materials, 64 (2021) 1801-1812; https://doi.org/10.1007/s40843-020-1554-y

[31] K. Hamad, M. Kaseem, H. W. Yang, et al, Express Polymer Letters, 9 (2015) 435-455; https://doi.org/10.3144/expresspolymlett.2015.42

[32] M. Mehrpouya, H. Vahabi, S. Janbaz, et al, Polymer, 230 (2021) 124080; https://doi.org/10.1016/j.polymer.2021.124080